ARTICLES
https://doi.org/10.1038/s41560-020-0576-y

nature energy

Dynamic stability of active sites in hydr(oxy)oxides for the oxygen evolution reaction

Dong Young Chung[1], Pietro P. Lopes[1], Pedro Farinazzo Bergamo Dias Martins[1], Haiying He[2], Tomoya Kawaguchi[1], Peter Zapol[1], Hoydoo You[1], Dusan Tripkovic[3], Dusan Strmcnik[1], Yisi Zhu[1], Soenke Seifert[4], Sungsik Lee[4], Vojislav R. Stamenkovic[1] and Nenad M. Markovic[1]✉

The poor activity and stability of electrode materials for the oxygen evolution reaction are the main bottlenecks in the water-splitting reaction for H_2 production. Here, by studying the activity–stability trends for the oxygen evolution reaction on conductive $M^1O_xH_y$, Fe–$M^1O_xH_y$ and Fe–$M^1M^2O_xH_y$ hydr(oxy)oxide clusters (M^1 = Ni, Co, Fe; M^2 = Mn, Co, Cu), we show that balancing the rates of Fe dissolution and redeposition over a MO_xH_y host establishes dynamically stable Fe active sites. Together with tuning the Fe content of the electrolyte, the strong interaction of Fe with the MO_xH_y host is the key to controlling the average number of Fe active sites present at the solid/liquid interface. We suggest that the Fe–M adsorption energy can therefore serve as a reaction descriptor that unifies oxygen evolution reaction catalysis on 3*d* transition-metal hydr(oxy)oxides in alkaline media. Thus, the introduction of dynamically stable active sites extends the design rules for creating active and stable interfaces.

Progress in the fundamental understanding of electrochemical interfaces, encompassing electrode materials (catalysts) and hydrated (solvated) ions in the double layer, has begun to revolutionize the development of alternative energy systems as a viable replacement to fossil fuel technology. At the core of this transition lies the oxygen evolution reaction (OER), an important electrochemical process in hydrogen production in water electrolysers[1], corrosion[2], metal/air batteries[3,4] and the synthesis of new chemicals from CO_2 reduction[5]. Not surprisingly, a wide variety of materials have been evaluated as active OER catalysts for water electrolysers, ranging from noble-metal oxides (for example, RuO_2 and IrO_2)[6,7], transition-metal oxides[8–10] and perovskite-type oxide structures[11,12] to 3*d* transition-metal-based hydr(oxy)oxides[13–17]. Together with changes to surface structure and composition, tuning the double layer through the use of covalent and non-covalent interactions is another effective strategy to improve catalytic activity[18,19], but it has not been consistently demonstrated for the OER[20,21]. Despite progress in increasing the activity, much less is known about the stability of these interfaces during oxygen evolution, an important aspect to guide the practical design of OER materials that require both high activity and stability.

Recently, it has been found that many OER active materials suffer severe dissolution during reaction[21–24], which implies that high activity in the OER is always accompanied by elevated metal dissolution rates (thermodynamic material instability)[25,26]. To take into account both activity and stability, the activity–stability factor (ASF)[27] was suggested as a metric that evaluates the ratio between the rate of O_2 production (activity) and metal dissolution (stability), measured simultaneously using the in situ inductively coupled plasma mass spectrometry (ICP-MS) method[28–30]. However, the fact that dissolution occurs indicates that the surface atoms are dynamic, which is inconsistent with the common view of the electrochemical interface as a static environment. The traditional view is that all the components are 'frozen' in space (static active sites), and only the reactants and products are mobile. This static view has begun to change as dynamic phenomena have been observed during the OER on metal oxide[31,32] and perovskite[12,33,34] surfaces, suggesting that activity and stability can be simultaneously enhanced. Thus, understanding the dynamic properties of the entire interface can open up the possibility of designing materials and interfaces that are no longer bound by severe thermodynamic instability.

Here, by learning from the functional links between activity and stability established for monometallic (M) and Fe-modified (Fe–M) hydr(oxy)oxide materials, we demonstrate that the creation of a dynamically stable interface (concomitant dissolution and redeposition of active sites) is possible after manipulation of both electrode and electrolyte components. The occurrence of dynamic active sites was verified by employing several experimental methods, both in situ and ex situ, in combination with isotopic labelling and ICP-MS experiments, confirming the formation of a highly active and dynamically stable catalyst. Further experimental and theoretical analysis suggests that this process is most effective (high ASF) when there is an optimum electrochemical interface, that is, a strong interaction between a stable host and a continuous exchange of active species, a concept that could be extended to other systems with modified hosts and active sites.

Activity and stability trends for monometallic MO_xH_y

We begin by establishing in situ the activity–stability trend, and thus ASF values, for the OER in alkaline media (0.1 M KOH) on well-defined monometallic 3*d* M hydr(oxy)oxide (MO_xH_y; M = Ni, Co, Fe) clusters deposited over Pt(111), as shown in Fig. 1. These MO_xH_y clusters have the benefits of well-defined surface area (roughness factor = 1), synthesis with good control of sub-monolayer coverage over the platinum surface (maximum at 50%, Fig. 1a)[19,35,36] as well as good electronic conductivity, needed for the determination of ASF (Supplementary Fig. 1). Because the presence of small amounts of impurities in the electrolyte can cause significant

---

[1]Materials Science Division, Argonne National Laboratory, Lemont, IL, USA. [2]Department of Physics and Astronomy, Valparaiso University, Valparaiso, IN, USA. [3]ICTM-Department of Electrochemistry, University of Belgrade, Belgrade, Serbia. [4]Advanced Photon Source, Argonne National Laboratory, Lemont, IL, USA. ✉e-mail: nmmarkovic@anl.gov

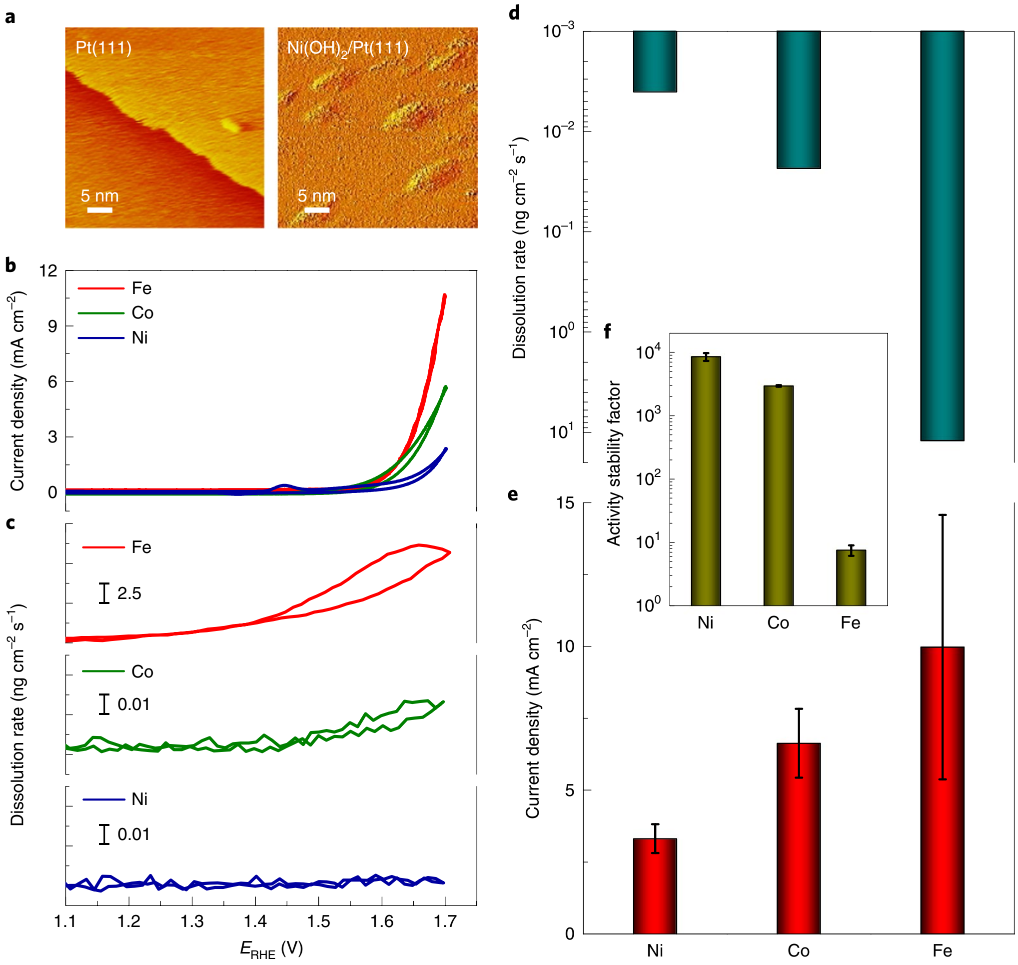

Fig. 1 | Activity–stability trend of 3*d* M hydr(oxy)oxides. a, STM images (40 × 40 nm) of Pt(111) and $Ni(OH)_2/Pt(111)$. **b**,**c**, Simultaneous in situ evaluation of OER activity (**b**) and monitoring of the metal dissolution rates (**c**) of MO_xH_y (M = Ni, Co, Fe) in purified 0.1 M KOH revealing that Fe hydr(oxy)oxide is the most active site for the OER in an alkaline environment, but also the most unstable. In **c**, scale bars are shown for each element. RHE, reversible hydrogen electrode. **d**–**f**, Summary of the activity–stability relationship for MO_xH_y (M = Ni, Co, Fe) obtained at 1.7 V, highlighting the dissolution rates (**d**) and current densities (**e**) for all three metal hydr(oxy)oxides, suggesting that Ni hydr(oxy)oxide is the most technologically relevant material within the monometallic series due its high stability, as indicated by its ASF (**f**). Measurements were taken at least three times and average values are presented with the standard error bar.

variations in the electrochemical performance, even more so in alkaline media[13,37–39], we chose to purify further high-purity commercial KOH by employing an electrolytic method (see Supplementary Note 1 and Fig. 2 for details).

Figure 1b,c shows the results of monitoring simultaneously the rates of O_2 production (current densities) and the rates of metal dissolution using our stationary probe rotating disk electrode (SPRDE) coupled to an ICP-MS spectrometer[28], revealing that FeO_xH_y is more active in the OER than CoO_xH_y and NiO_xH_y (ref. [40]). Although the activity is the highest for the Fe-containing substrate, its potential-dependent dissolution rate at OER potentials is three orders of magnitude higher than those observed for the Co- and Ni-based hydr(oxy)oxides (Fig. 1d, approx. 12.1, 0.023 and 0.004 ng cm^{-2} s^{-1}, respectively). By comparing the activity and stability at 1.7 V, the stability trend observed is $NiO_xH_y > CoO_xH_y >> FeO_xH_y$, which is the exact opposite trend measured for OER activity, $NiO_xH_y < CoO_xH_y < FeO_xH_y$ (Fig. 1e).

As a consequence of its higher dissolution rate, Fe hydr(oxy)oxide shows a significant drop in OER activity during its initial five cycles (poor activity retention) followed by a decrease in the amount of Fe dissolution in every consecutive cycle (Supplementary Fig. 3), a direct consequence of active-site depletion at the electrode surface[41,42]. Similar results were obtained from chronoamperometry measurements at constant voltage (1.7 V, 1 h), indicating that severe dissolution of Fe undermines its use as an OER catalyst, whereas NiO_xH_y shows the highest stability without any appreciable activity loss (Supplementary Fig. 3). These results serve as the basis for activity–stability relationships on M hydr(oxy)oxides, best summarized by the ASF values calculated at 1.7 V (Fig. 1f). As a rule of thumb, the ASF evaluates the extent to which a material produces O_2 molecules (specific for the OER) for a given amount of dissolution of the active site. Therefore, the higher the ASF of a material, the more O_2 is produced per dissolved active site. The conclusion after evaluation of the ASF values for the FeO_xH_y, CoO_xH_y and NiO_xH_y sites is that the Ni-based hydr(oxy)oxide is the most promising durable catalyst for O_2 production in this series, as the elevated ASF reflects its extremely high stability despite its poor OER activity. Further evaluation of the Faradaic efficiency for O_2 production (FE_{oxygen}) on MO_xH_y was performed by using the rotating ring-disk electrode (RRDE) method (Supplementary Fig. 4). The high FE_{oxygen} values for Ni and Co hydr(oxy)oxide (over 99%) indicate that most of the current originates from O_2 evolution and not side reactions such as H_2O_2 production or from corrosion currents. On the other hand, the measured Faradaic efficiency of FeO_xH_y shows poor stability

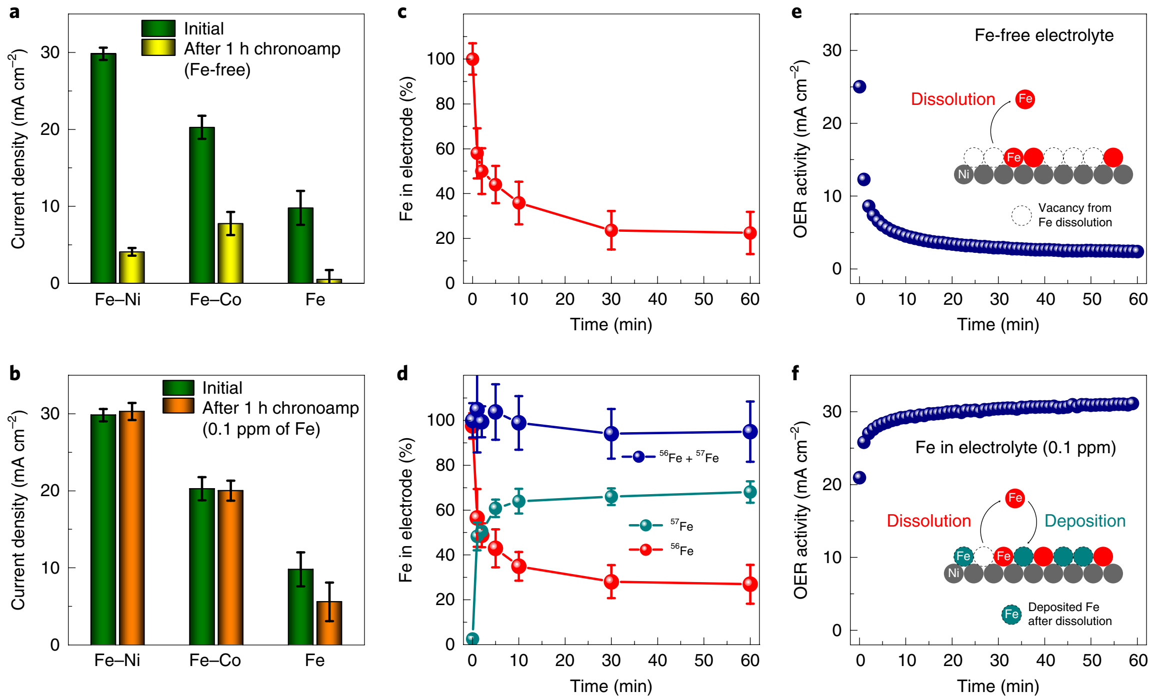

Fig. 2 | Activity–stability trend of Fe–M hydr(oxy)oxides and observation of dynamic Fe exchange by isotopic labelling experiments. **a**,**b**, Summary of the results of the activity–stability study of Fe–M hydr(oxy)oxides during chronoamperometry experiments at 1.7 V for 1 h in ‘Fe-free’ purified KOH (**a**) and in a KOH solution containing 0.1 ppm Fe (**b**), revealing the high dependence of OER activity retention on the presence of Fe in the electrolyte. **c**–**f**, The total amount of Fe in the Fe-NiO$_x$H$_y$ electrode (**c**,**d**) and OER activity (**e**,**f**) during chronoamperometry measurements at 1.7 V show Fe dissolution from the electrode surface accompanied by OER activity loss in the ‘Fe-free’ electrolyte (**c**,**e**). The schematic diagram in **e** depicts the dissolution process. Similar chronoamperometry experiments performed in electrolyte containing 0.1 ppm ^{57}Fe (**d**,**f**) reveal Fe dynamic exchange (dissolution and redeposition) at the interface during OER catalysis, as the quick dissolution of ^{56}Fe from the electrode is followed by immediate redeposition of ^{57}Fe from the electrolyte. The dynamic exchange preserves the overall Fe content at the electrode surface, which is reflected in the high OER activity that does not decrease during the course of the experiment. The schematic diagram in **f** depicts both the Fe dissolution and redeposition processes, with balanced rates brought about by the trace level of Fe in the electrolyte.

(~88%), which is in good agreement with its ASF value, and no formation of H_2O_2 (Supplementary Fig. 5).

Activity and stability trends for Fe-MO$_x$H$_y$

As Ni- and Co-based hydr(oxy)oxide systems incorporating Fe have been shown to display significant activity in alkaline media[13,37], we added Fe nitrate to the purified electrolyte to form Fe–MO$_x$H$_y$ (Fe–Ni and Fe–Co) and compared their activity–stability trends. Scanning tunnelling microscopy (STM) revealed that the cluster height increases slightly with respect to the monometallic systems (Supplementary Fig. 6), suggesting that Fe is selectively adsorbed on the Ni and Co hydr(oxy)oxide substrates. Further quantification of Fe incorporation revealed an Fe content of 15 to 28% by weight in the Co- and Ni-containing MO$_x$H$_y$ clusters, respectively (Supplementary Fig. 6).

The OER activity trend for Fe–MO$_x$H$_y$ (Fig. 2a and Supplementary Fig. 7) is reversed when compared with the results for monometallic systems (Fig. 1), decreasing in the order Fe–NiO$_x$H$_y$ > Fe–CoO$_x$H$_y$ > FeO$_x$H$_y$. At 1.7 V, the current density on bimetallic Fe–NiO$_x$H$_y$ is nine times higher than that observed with pure NiO$_x$H$_y$, and it is enhanced about three times on Fe–CoO$_x$H$_y$ clusters in comparison with pure CoO$_x$H$_y$, highlighting the fact that a small amount of Fe in a material can significantly enhance its OER activity and that current enhancement originates from actual O_2 evolution (Supplementary Fig. 8). In addition, this Fe effect is observed regardless of support (Pt(111), glassy carbon, nickel or cobalt metal surfaces), indicating that the MO$_x$H$_y$–Fe interaction is key to promoting the OER (Supplementary Fig. 9).

Together with the trends in catalytic activity, it is important to establish the stability trends for bimetallic hydr(oxy)oxides so that ultimately we can determine their technological relevance based on the ASF values. Surprisingly, the trend in stability, as measured by the activity retention for the Fe-containing MO$_x$H$_y$ clusters, is highly dependent on the presence of trace levels of Fe in the electrolyte (Fe^{n+}(aq.) = 0.1 ppm). In pure KOH solutions, the activities of the Fe–NiO$_x$H$_y$ and Fe–CoO$_x$H$_y$ samples show a remarkable deactivation after just 1 h of potential hold at 1.7 V (Fig. 2a), reducing the initial high activities to almost the same levels as the monometallic hydr(oxy)oxides (Supplementary Fig. 10). However, the addition of Fe^{n+}(aq.) to the electrolyte effectively prevents activity loss under the same test conditions (Fig. 2b).

On the one hand, in situ measurement of dissolution rates from Fe–NiO$_x$H$_y$ during potential cycling (Supplementary Fig. 11) shows that the total amount of Ni dissolution is still negligible. However, Fe still leaches from NiO$_x$H$_y$ at a rate almost two orders of magnitude greater than Ni itself, although not as fast as observed from the pure monometallic hydr(oxy)oxide system (Fig. 1). The same trend is observed in Fe–CoO$_x$H$_y$ (Supplementary Fig. 11), suggesting that the lack of stability (poor activity retention) in the Fe–MO$_x$H$_y$ systems when Fe^{n+}(aq.) is not present in the electrolyte is related to the dissolution of Fe active sites, notably due the depletion of the initial Fe content from the electrode surface. On the other hand, evaluation of Fe dissolution when the electrolyte contains Fe^{n+}(aq.) reveals the same dissolution process as shown in Supplementary Fig. 11, although the OER activity levels remain elevated and unchanged throughout the experiment.

From the results of the activity and stability studies of M and Fe–M hydr(oxy)oxides, there are three important features to emphasize. First, during the OER, Fe active sites are very unstable, regardless of whether they are present in Fe or as Fe–M hydr(oxy)oxides. Second, despite the high initial activity, the subsequent activity decay observed for Fe-containing MO_xH_y systems is related to Fe depletion through dissolution. Third, preserving the high activity levels can be achieved only when the electrolyte contains Fe^{n+}(aq.) even though Fe dissolution from the surface will still occur (Supplementary Fig. 12). The fact that these results indicate that the material itself is not absolutely stable, but OER activity can be sustained over time, implies that a significant Fe dynamic exchange is continuously taking place at the interface.

To confirm this dynamic Fe exchange at the interface we measured the total amount of ^{56}Fe and ^{57}Fe in the electrode using ICP-MS at different stages of the chronoamperometry experiments (see details in the Methods section), providing information about the kinetics of dissolution as well as the kinetics of Fe^{n+}(aq.) redeposition. Therefore, by starting with ^{56}Fe in the electrode and ^{57}Fe in the electrolyte, any loss of ^{56}Fe and gain of ^{57}Fe can be traced back to dissolution and deposition events occurring during the OER, respectively. As a control experiment, Fig. 2c shows potential hold experiments on Fe-NiO_xH_y in which a continuous decrease of Fe in the electrode during polarization is observed, followed by OER deactivation (Fig. 2e). This is in line with the results shown in Fig. 2a, emphasizing that Fe dissolution decreases the number of active sites on the electrode surface. However, when 0.1 ppm ^{57}Fe is in the electrolyte ($^{57}Fe^{n+}$(aq.)), dissolution of ^{56}Fe occurs at the same rate as in Fig. 2c (~0.53 ng cm^{-2} s^{-1}), but the amount of ^{57}Fe in the electrode increases at a similar rate to the ^{56}Fe loss (~0.56 ng cm^{-2} s^{-1}, Fig. 2d). This results in an overall Fe content, ^{56}Fe + ^{57}Fe, that is constant throughout the experiment. Note that half of the ^{56}Fe in the electrode has already exchanged with ^{57}Fe in less than 1 min and ^{57}Fe/Fe reaches 70% after 1 h, confirming that rapid Fe dissolution and redeposition happens at the interface during OER. Interestingly, as a consequence of dynamic exchange, the overall Fe content in the electrode remains constant, preserving the total number of active sites for the OER, and thus eliminating any catalytic deactivation (Fig. 2f). This further supports the fact that Fe is an intimate part of the active site for the OER in alkaline media when combined with Ni or Co hydr(oxy)oxides.

The ability of Fe to promote OER activity on Ni and Co hydr(oxy)oxides has been reported before, but the origin of such activity enhancement remains elusive. Many reports identify Ni, promoted by Fe, as the active sites[43,44], whereas others indicate that Fe could be the source of the OER enhancement[45,46], with relevant considerations of the role of plane or edge sites and substitutional doping[47–50]. Given the trends observed for MO_xH_y (Fig. 1), it is clear that pure Ni cannot be the active site, strongly suggesting that Fe acts as the active site. This assertion is further supported by in situ X-ray absorption near-edge spectroscopy (XANES) analysis (Supplementary Fig. 13), and consideration of other electrocatalytic reactions, such as the hydrogen evolution reaction (Supplementary Fig. 14), preclude Ni or Co as the effective active sites (electronically modified by Fe) for the OER[51]. However, it is clear that Fe species at the interface together with Ni and Co oxide hosts are critical for achieving high levels of O_2 production.

Dynamically stable Fe as active site for oxygen evolution

By controlling the Fe^{n+}(aq.) concentration in the electrolyte, increasing the Fe^{n+}(aq.) content above 0.1 ppm does not lead to any further increase in OER activity (Fig. 3a), nor an increase in the amount of Fe incorporated into either the Ni or Co hydr(oxy)oxide (Fig. 3b). These results indicate that OER activity is linked to the amount of Fe present in the MO_xH_y and that there is an Fe saturation coverage (monolayer, ML) for each surface. The linear relationship between OER and Fe coverage reveals that the factors contributing to the promotion of the OER on Fe–NiO_xH_y and Fe–CoO_xH_y are not unique to each bimetallic system (Fig. 3c), but rather, form part of a general description of the active sites linked to the number of dynamic stable sites (Fe).

Density functional theory (DFT) calculations reveal that the $\Delta\bar{G}_{\text{Fe}-\text{M}}$ values (Fe average adsorption free energy on MO_xH_y sites) are strongly dependent on the substrate nature (Supplementary Fig. 15). In simple terms, a more negative $\Delta\bar{G}_{\text{Fe}-\text{M}}$ value implies a higher Fe saturation coverage on MO_xH_y. Figure 3d summarizes the Fe adsorption free-energy trends for the Ni, Co and Fe MO_xH_y substrates, revealing that Fe adsorption on FeO_xH_y is unfavourable and that NiO_xH_y shows the strongest interaction with Fe^{n+}(aq.) (−0.69 eV at a coverage of 0.25 ML), and consequently the highest Fe coverage in this series, providing a good match with the experimental values (Supplementary Fig. 16). Furthermore, the rate of Fe dissolution depending on the host ($FeO_xH_y >> CoO_xH_y > NiO_xH_y$) is also affected by the Fe adsorption energy (Fe < Co < Ni), suggesting that a strong interaction of MO_xH_y with Fe not only leads to a higher number of active sites, but also stabilizes these active sites.

By taking into consideration the Fe dynamic exchange (Fig. 2) and the correlation of OER activity with the number of Fe (Fig. 3), we propose that O_2 evolution catalysis occurs at a number of dynamically stable active sites (N^*), which is distinguished from the conventional number of active site (N) considered under static conditions (see Supplementary Note 6). The average number of dynamically stable active Fe sites $\left(N^*_{\text{Fe}}\right)$ can be estimated from equation (1), with equation (2) showing the OER activity (i_{OER}) dependence on the number of dynamically active Fe sites:

$$N^*_{\text{Fe}} = \left(\frac{1}{1+\mathrm{e}^{\frac{\Delta G_{\text{Fe}-\text{M}}}{RT}}}\right)\left(\frac{r_{\text{dep}}C^0_{\text{Fe}}}{r_{\text{dep}}C^0_{\text{Fe}}+r_{\text{diss}}}\right) \tag{1}$$

$$i_{\text{OER}} = i^0 N^*_{\text{Fe}} \exp\left(\frac{\beta F(E-E^0)}{RT}\right) \tag{2}$$

where $\Delta G_{\text{Fe}-\text{M}}$ is the adsorption energy between Fe and the M hydr(oxy)oxide surface, $r_{\text{dep}}C^0_{\text{Fe}}$ is the overall rate of Fe deposition and r_{diss} is the rate of Fe dissolution during the OER (given in ng cm^{-2} s^{-1}), i_{OER} is the OER current density, i^0 is the exchange current density, β is the symmetry factor[52], E is the applied potential, E^0 is the equilibrium potential for OER and F, R and T indicate the Faraday constant, ideal gas constant and temperature, respectively. At a given potential, the kinetics of oxygen evolution is determined by the number of dynamic active sites N^*_{Fe}, equation (1) incorporating the process of Fe redeposition and the interaction with the hydr(oxy)oxide host.

From equations (1) and (2), the maintenance of high N^*_{Fe} within a host to enable stable OER activity requires two conditions. First, the electrolyte must contain Fe^{n+}(aq.) species to a sufficiently high level that the rate of redeposition can be equal to or much greather than the rate of dissolution ($r_{\text{diss}} \ll r_{\text{dep}}C^0_{\text{Fe}}$, Fig. 2f). This will ensure a high enough average Fe coverage on the electrode. Second, the dynamic Fe species must interact with the clusters at the electrode surface where they can reside and catalyse O_2 production before they dissolve. If the rate of dissolution is too high or the rate of Fe deposition does not reach that of dissolution, the overall number of dynamic Fe species will decrease, resulting in activity decay ($r_{\text{diss}} >> r_{\text{dep}}C^0_{\text{Fe}}$, Fig. 2e).

Considering that continuous elemental dissolution and redeposition occurs during the OER, our ‘dynamic stable active site (Fe)/host pair’ concept could be seen as similar to the self-healing mechanism suggested in previous work[31,32]. Unlike self-healing, the regeneration of the active sites in a dynamic stable state necessarily requires a ‘specific host’ with a strong interaction with the dynamic

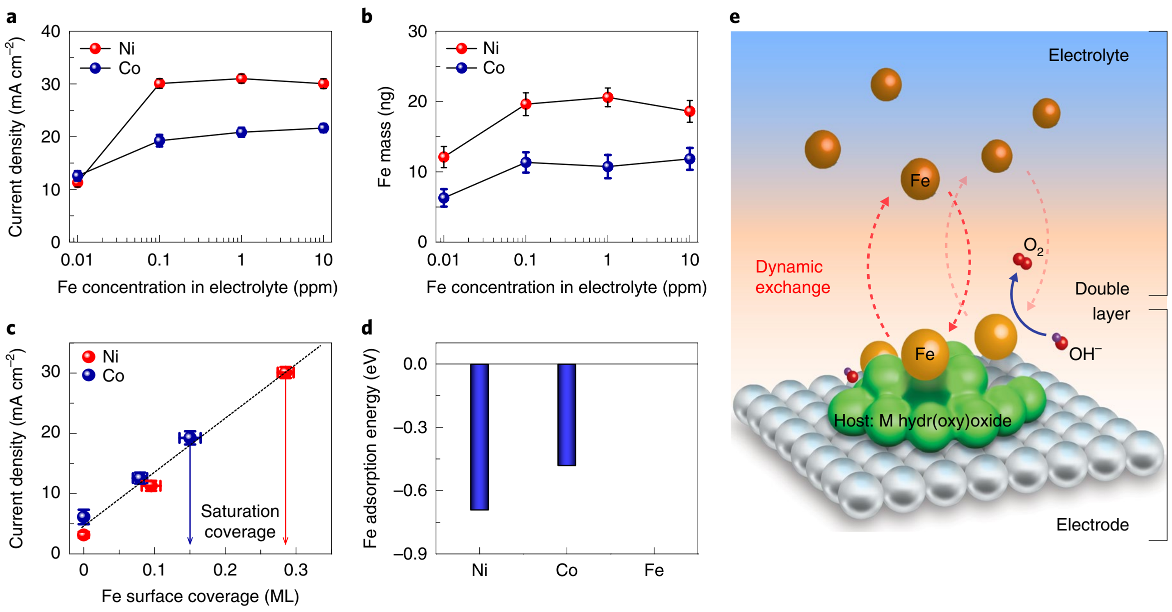

Fig. 3 | Dynamically stable Fe as active site for OER. a,**b**, Effect of Fe concentration in the electrolyte on OER activity (**a**) and Fe mass retained (**b**) in Fe–Ni and Fe–Co hydr(oxy)oxide clusters, revealing that Fe adsorption saturates at high Fe concentrations (above 0.1 ppm). **c**, The correlation between absolute OER activity and Fe coverage on both Fe–Ni and Fe–Co hydr(oxy)oxides indicates that OER catalysis enhancement increases linearly with average Fe coverage as a result of stronger Fe–M hydr(oxy)oxide interactions. Note that the arrows indicate maximum Fe surface coverage on the Ni (red) and Co (blue) substrates. Measurements were taken at least three times and average values are presented with the standard error bar. **d**, DFT calculations of the average adsorption free energies for Fe on M hydr(oxy)oxide at a coverage of 0.25 ML. The adsorption free energy of the Fe complex on FeOOH is set to zero because it is unfavourable. **e**, Schematic diagram of the 'dynamically stable' active-site/host pair at the electrode/electrolyte interface, highlighting the role of M hydr(oxy)oxide as a suitable host for Fe species to stay at the interface long enough to catalyse the conversion of OH^- into O_2 molecules, with the presence of Fe in the electrolyte ensuring that Fe species can return to the interface and redeposit at hydr(oxy)oxide sites.

'active sites'. In this scenario, Fe species would be the active sites that can be dynamically stable only because of their interaction with stable NiO_xH_y or CoO_xH_y clusters. By contrast, the simple self-healing process of Fe on FeO_xH_y (Fig. 2a,b) is not sufficiently effective for Fe to be fully adsorbed on the electrode surface and unleash its OER catalytic activity. Unlike static interfaces, the dynamic stable condition counterbalances the intrinsic high dissolution rate of the active sites by promoting their redeposition through tailored electrode–electrolyte interactions.

From the point of view of OER activity, there are two routes to maximize catalysis. First, increasing the absolute number of dynamic Fe active sites can be achieved by increasing the surface area of the host material. Although this strategy seems trivial, it is the only pathway available if the material properties related to Fe adsorption ($\Delta G_{\text{Fe–M}}$) cannot be tuned. This is shown when a steady increase in the amount of NiO_xH_y deposited on Pt(111), for instance, results in an increase in the absolute OER activity both in pure KOH as well as in electrolyte containing Fe^{n+}(aq.) at saturation levels. Despite these increases in absolute activity, the ratio between OER currents with and without Fe^{n+}(aq.), called the activity enhancement factor (I_{Fe}/I), remains the same for all amounts of Ni hydr(oxy)oxides (Supplementary Fig. 18).

Second, the number of dynamic Fe species can be increased by tuning the Fe adsorption ($\Delta G_{\text{Fe–M}}$) on the host materials. Based on the DFT trend in which $\Delta G_{\text{Fe–M}}$ shows an inverse relationship with the bond energy ($\Delta G_{\text{M–O}}$; Supplementary Fig. 15), we screened other 3*d* transition metals in an attempt to find MO_xH_y host candidates better than NiO_xH_y (Supplementary Fig. 19). Figure 4a shows that the elements to the left of Fe in the periodic table do not show any OER activity enhancement with Fe. Because the M–O bond becomes stronger towards the left of the periodic table[53], Fe adsorption is unfavourable. In the opposite direction (to the right of Fe), activity enhancement is clearly observable and is the highest for CuO_xH_y. Although Cu hydr(oxy)oxide shows the highest activity enhancement factor, its high dissolution rate prevents its use as a practical MO_xH_y host (Supplementary Fig. 20).

By doping the Ni hydr(oxy)oxide cluster with various other 3*d* transition metals as dopants (Mn, Co and Cu) we were able to further tune the Fe adsorption energy and consequently improve OER activity levels. Following the trend in the enhancement factor on pure 3*d* MO_xH_y, doping NiO_xH_y with Cu atoms ($NiCuO_xH_y$, see Supplementary Fig. 21) leads to superior OER activity (40.5 mA cm^{-2}) in KOH containing 0.1 ppm Fe, which is 1.4 times higher than that of NiO_xH_y with Fe^{n+}(aq.) (Fig. 4b). Furthermore, the activity enhancement factor (I_{Fe}/I) of NiCu hydr(oxy)oxide surpasses that of pure NiO_xH_y, although it is still lower than that of pure CuO_xH_y. The increase in Fe surface coverage revealed by ICP-MS and supported by DFT analysis suggests that the high activity of $NiCuO_xH_y$ clusters originate from the increase in Fe adsorption energy, and consequently higher average Fe coverage, making it the most suitable Fe host (Supplementary Fig. 22). This trend is further validated by the observed linear relationship between OER activity and the number of dynamic Fe species measured on the NiMn and NiCo hydr(oxy)oxides (Fig. 4c and Supplementary Fig. 23). Although further promotion of OER activity can occur through a synergistic interaction of the support (MO_xH_y) with Fe, caused by electronic (or geometric) effects or a possible new reaction mechanism/pathway[45,49,50], our observations strongly support the idea that the number of dynamic stable sites (Fe) can be regarded as a general descriptor of the active sites, as described in equation (2). It is likely that the Fe–M adsorption energy, which determines the saturation coverage of Fe on a given MO_xH_y, may be more relevant than the M–O adsorption energy as activity descriptor[6].

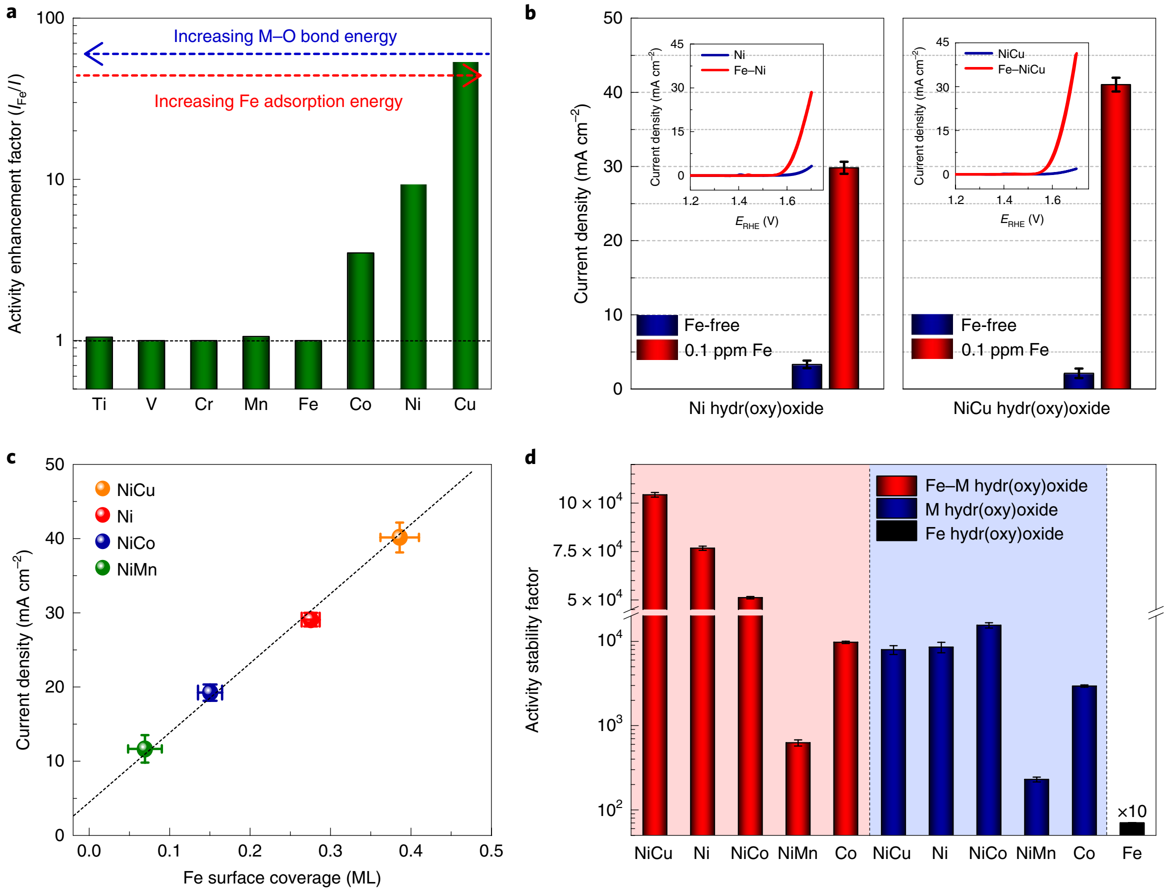

Fig. 4 | Interface (dynamic active species/host pair) design for highly active and durable system. a, The activity enhancement trend for Fe incorporation into 3*d* transition-metal hydr(oxy)oxides indicates that the Fe interaction (Fe adsorption energy increases with each element, from left to right (red dashed line)) shows an inverse correlation with the M–O bond energy (blue dashed line). **b**, OER activity of Ni (left) and NiCu (right) hydr(oxy)oxides in pure KOH and KOH containing 0.1 ppm Fe. The insets show the potential–current density plots in the OER region. **c**, The correlation between absolute OER activity with Fe surface coverage on NiM (Cu, Co, Mn) and Ni hydr(oxy)oxides indicates that OER catalysis enhancement increases linearly with average Fe coverage. The plot clearly demonstrates that 'dynamic stable Fe' is a general descriptor for OER activity. **d**, A comparison of the ASF values of different Fe–M and M hydr(oxy)oxides reveals that engineering dynamic active-site/host pairs with a high number of dynamic Fe species and a stable host is a key design principle. Measurements were taken at least three times and average values are presented with the standard error bar.

From a stability point of view, in situ ICP-MS indicates that Cu in NiCu hydr(oxy)oxide is more stable in the OER potential window than pure CuO$_x$H$_y$, although it does start to dissolve at potentials above 2.1 V versus RHE (Supplementary Fig. 24). Constant current density measurements performed at 10 mA cm^{-2}, which is considered as a benchmark for OER stability[54], and high Faradaic efficiency (>99%) also indicate a superior electrochemical stability without appreciable activity loss (Supplementary Fig. 24), verifying that Fe–NiCuO$_x$H$_y$ shows not only high material stability (decreased rates of dissolution), but also superior catalytic stability (stable chronoamperometry).

Finally, our observations suggest a way to maximize the ASF values for OER materials to achieve high activity and stability simultaneously (Fig. 4d). The Fe-containing samples (red bars in Fig. 4d) show high ASF values compared with the 'Fe-free' samples (blue bars in Fig. 4d) due to the high activity gained from hosting Fe active sites. The use of Ni and Cu as hydr(oxy)oxide hosts leads to a better ASF value due to simultaneous improvement in the activity enhancement factor (stronger Fe adsorption) and the prevention of Cu dissolution due to Ni–Cu interactions. This stabilization effect is shown with NiCoO$_x$H$_y$, as it displays an elevated ASF value due to the prevention of Co dissolution by NiO$_x$H$_y$, but CoO$_x$H$_y$ and NiCoO$_x$H$_y$ have similar OER activities (Supplementary Fig. 25). As a result, active-species/host pairs overcome the limitations placed on the ASF by material instability of both active sites and additional atoms present to tailor Fe–MO$_x$H$_y$ interactions.

Conclusions

In summary, we have investigated activity–stability trends for the OER on conductive M (M = Ni, Co, Fe) and Fe–M hydr(oxy)oxide clusters and found dynamically stable Fe as a result of dissolution and redeposition at the electrolyte/host interface, which provides a general description for OER activity and stability. By realizing that this dynamic stability overcomes the limitations imposed by the thermodynamic instability of oxide materials at OER potentials, we propose that the design of new materials should be focused on attaining a high number of dynamically stable active sites within a stable host under solid/liquid interfacial control. We have demonstrated an example of how these design rules can increase Fe use, by preparing Fe–NiCu hydr(oxy)oxide with higher OER activity than the Cu-free material. In the future, the design of new active-site/host pairs may lead to the discovery of new (electro)chemical interfaces that are simultaneously highly active and highly stable for the OER.

Methods

Chemicals. High-purity, trace-analysis grade potassium hydroxide hydrate (Trace SELECT, Fluka) was further purified as discussed below. All transition metals used here, Ni, Co and Fe nitrate hexahydrates and Cu and Mn nitrate hydrates (99.995% metal basis, Sigma Aldrich), were employed as supplied. Electrolytes were prepared with Milli-Q Millipore deionized (DI) water. All gases (argon, oxygen and hydrogen) were of 99.9999% quality (Airgas).

Electrolyte purification and confirmation of electrolyte purity. Electrolyte (KOH) purification to control the cation concentration was conducted by prolonged electrolysis (5 d) using Ni wire (3.925 cm^2, Puratronic, 99.999%, Alfa Aesar) as both working and counter electrode, motivated by previous reports[13,37]. Electrolysis purification was conducted inside a plastic cell made out of fluoropolymer material to avoid contamination from glass components. We confirmed the purity of the electrolyte by electrochemical methods using Pt(111) cyclic voltammetry (CV). Based on a previous report[38], small amounts of cation (Ni, Co and Fe) in alkaline electrolyte affect the CV shape of Pt(111) significantly. Inspired by the high sensitivity and clear observation of a cation effect on electrochemical performance, we compared the CV of Pt(111) after ten potential cycles from 0.05 to 0.9 V with the initial CV of Pt(111) obtained in our purified electrolyte (for detailed information see Supplementary Fig. 2 and Note 1). To maximize the mass transport of any possible impurities in the electrolyte, CV was performed with a rotating electrode at 1,600 r.p.m. By our method, in purified KOH, there was no change before and after CV cycling, indicating that our method can efficiently remove any trace level of impurities that could affect electrochemical performance.

Extended surface electrode preparation and metal hydroxide deposition. Pt(111) single-crystal electrode (6-mm diameter) was prepared by inductive heating for 7 min at ~1,100 °C in a flow of argon/hydrogen (3% hydrogen). The annealed crystal was cooled slowly to room temperature under an inert atmosphere and immediately covered with a drop of DI water. To screen the candidates for host materials, a 6-mm-diameter metal electrode was used. Before the experiments, the electrode was prepared by mirror polishing with alumina powder and then immersed in KOH solution to reach saturation conditions. The electrodes were then assembled into a rotating disk electrode (RDE). Polarization curves were recorded in argon-saturated electrolyte. By potential cycling between the underpotential deposition of hydrogen (H_{upd}) and hydroxide adsorption (OH_{ad}) region in the presence of 1–100 ppm transition-metal nitrate, metal hydr(oxy)oxide layers were deposited on Pt(111). The surface coverage of the MO_xH_y layer was controlled by the number of potential cycles and concentration of the cation. The mass loading of hydr(oxy)oxide was confirmed by ICP-MS and repetitive analysis was conducted at least three times for each element. Fe–M hydroxide samples were prepared by spike experiments with 0.1 ppm Fe nitrate hexahydrate (the ^{56}Fe/^{57}Fe ratio was 92:2 and is denoted as ^{56}Fe in the manuscript) in the electrolyte. The Fe surface coverage (ML) on Fe–M hydr(oxy)oxides was calculated from the mass ratio between Fe and M (Ni, Co, Cu and Mn) based on the STM and CV results. The mass ratios of the dopant M in NiM samples were 25.8 (Cu), 26.2 (Co) and 24.8% (Mn).

Electrochemical measurements. Electrochemical measurements were controlled using an Autolab PGSTAT 302N potentiostat. A typical three-electrode configuration in a fluoropolymer-based cell was used to avoid contamination from glass components in the alkaline media. To avoid any contamination from previous experiments, the cell was thoroughly rinsed with DI water and then DI water was boiled in the cell before every experiment. A glassy carbon rod and Ag/AgCl were used as the counter and reference electrodes, respectively. To avoid any contamination from the glassy carbon counter electrode as a result of its use in previous experiments, the glassy carbon was thoroughly washed with 1 M HCl and immersed in boiling DI water before every experiment. OER measurements were carried out by cycling the electrode up to 1.7 V versus RHE. The *iR* drop compensation was conducted during measurements. The current densities reported in this paper were normalized by the geometric area of the Pt(111) substrate (0.283 cm^2). Potential hold experiments were also carried out on the hydroxide/Pt(111) systems to study the stability at 1.7 V versus RHE. Constant current density measurements of Fe–NiCu hydr(oxy)oxide were conducted in KOH containing 0.1 ppm Fe at 10 mA cm^{-2}. All electrochemical measurements were conducted in 'Fe-free' electrolyte purified by our protocol unless indicated otherwise in the manuscript. For the isotopic-labelling experiment, 0.1 ppm Fe in KOH was prepared with the ^{57}Fe precursor from Alfa Aesar (the ^{56}Fe/^{57}Fe ratio was 3:95.5 and is denoted as ^{57}Fe in the manuscript). Because the background value was too high to observe Fe dynamics if 0.1 ppm Fe was present in the electrolyte, we analysed the Fe isotopes in the Fe–M hydr(oxy)oxides by preparing the electrodes with ^{56}Fe and conducting electrochemical analysis in ^{57}Fe-containing KOH electrolyte. To quantify the amount of Fe (^{56}Fe and ^{57}Fe) in the electrode during chronoamperometry measurements, the electrode (Fe–M hydr(oxy)oxide) was thoroughly dissolved in 0.1 M HNO_3 and analysed by ICP-MS. All electrochemical measurements were performed at least three times and average values are presented with the standard error bar.

STM and atomic force microscopy measurements. For cluster-shape and height-information analyses, STM images were acquired with a Digital Instruments Multi-Mode Dimension STM controlled by a Nanoscope III control station using Pt(111), Ni hydr(oxy)oxide on Pt(111) and Fe–Ni hydr(oxy)oxide on Pt(111). During the STM measurements, the microscope supporting the sample was enclosed in a pressurized cylinder under a CO atmosphere. Atomic force microscopy (AFM) images were collected in soft tapping mode (Bruker Dimension ICON) to measure the topography of NiCu hydr(oxy)oxide deposition on Pt(111). The AFM data were processed using the GWYDDION (version 2.53) software package.

In situ XANES measurements. XANES measurements were performed at the 12-ID-C beamline of the Advanced Photon Source of the Argonne National Laboratory. A custom-made in situ electrochemical X-ray cell with a 6-mm diameter of Pt(111) single crystal and a Ag/AgCl reference electrode was used in grazing-incidence geometry (digital photograph images for the in situ set-up are presented in Supplementary Fig. 9a). The experimental geometry was similar to that used previously in grazing-incidence fluorescence X-ray absorption spectroscopy (GIF-XAS)[55]. The grazing angle of incidence was fixed at the total external reflection angle of the X-rays (~0.5°) for the Pt(111) substrate. Under this condition, the electric field at the surface is enhanced to achieve a maximum sensitivity of the elements on the surface. A Vortex detector (Hitachi High-technologies Science America) with an active area of 1 cm^2 and an energy resolution of ~120 eV was used. A cobalt filter for Ni K-edge XANES and a Mn filter for Fe K-edge XANES were used and the detector was positioned at 90° to the horizontally polarized incoming X-rays to suppress elastic scattering. Then, the detector distance was set to ~3 cm from the surface to optimize the signal-to-background ratio. The spectra were normalized by the incident X-ray intensity and processed using the ATHENA software (Ifeffit 1.2.12).

X-ray photoelectron spectroscopy analysis. X-ray photoelectron spectroscopy analysis was conducted using an Ommicron EA-125 hemispherical energy analyser with an Al K_α X-ray source.

In situ ICP-MS coupled to SPRDE. The set-up for ICP-MS analysis coupled to SPRDE has been described in a previous report[28]. Metal ions such as Fe (56 and 57 AMU), Co (59 AMU), Mn (55 AMU), Cu (64 AMU) and Ni (60 AMU) were detected with a PerkinElmer NexION 350S spectrometer coupled to an SPRDE. Electrochemical measurements were conducted in the same way as described in the Electrochemical measurements section.

ASF calculation. The ASF values were calculated according to our previous report[27] as follows:

$$\mathrm{ASF} = \left.\frac{I - S}{S}\right|_{\eta}$$

where I indicates the rate of O_2 production (equivalent to the OER current density) and S indicates the rate of host metal dissolution (equivalent to the dissolution current density) at constant overpotential η. When dynamic stable Fe is incorporated into the host materials (Fe-containing KOH), the ASF (dynamic Fe–M hydr(oxy)oxide) values are simply the ASF values obtained for the corresponding values without Fe multiplied by the activity enhancement factor $\left(\frac{I_{\mathrm{Fe}}}{I}\right)$.

$$\mathrm{ASF(dynamic\ Fe-M\ hydr(oxy)oxide)} = \mathrm{ASF(without\ Fe)} \times \left(\frac{I_{\mathrm{Fe}}}{I}\right)$$

RRDE measurement for quantifying O_2 production and calculation of $\mathrm{FE}_{\mathrm{oxygen}}$. To quantify the actual production of O_2 and calculate the $\mathrm{FE}_{\mathrm{oxygen}}$, we used the RRDE method with a platinum ring. To calibrate the collection efficiency in the gas evolving reaction, the hydrogen evolution reaction was used (see detailed discussion in Supplementary Note 2). To calculate $\mathrm{FE}_{\mathrm{oxygen}}$, we measured each sample twice with different ring potentials (1.1 V for H_2O_2 and 0.4 V for O_2). The production of O_2 was monitored using a ring potential of 0.4 V versus RHE because at this potential the O_2 reduction is in diffusional control while preventing H_{upd}, which would allow the $2e^-$ pathway during O_2 reduction. For H_2O_2, we chose 1.1 V as it is a high enough potential for H_2O_2 oxidation (diffusion-limiting region) while being below the thermodynamic potential of O_2 evolution (1.23 V). $\mathrm{FE}_{\mathrm{oxygen}}$ is defined as follows:

$$\mathrm{FE}_{\mathrm{oxygen}} = \frac{\mathrm{O_2\ evolution\ current\ (ring\ current)}}{\mathrm{Total\ current\ (disk\ current)}} \times \mathrm{Collection\ efficiency}$$

Computational methods. Electronic structure calculations were performed within the framework of DFT with periodic boundary conditions using the VASP program[56]. All surface calculations were carried out using the implicit solvation model implemented in the VASPsol package and including the effects of electrostatics, cavitation and dispersion on the interaction between solute and solvent[57,58]. The Perdew–Burke–Ernzerhof (PBE) exchange-correlation functional[59] and the van der Waals interactions described by a pairwise force field using the DFT-D2 method of Grimme[60] were used for all calculations. The projector augmented wave method and plane wave basis sets were used with energy cut-offs of 520 eV for full cell geometry optimization and 400 eV for geometry optimization with fixed cell parameters. Transition-metal elements were treated by the PBE + U method with $U_{\mathrm{eff}} = 5.5$, 4.4 and 3.3 eV for Ni, Co and Fe, respectively[61]. Transition-metal oxyhydroxide MOOH (M = Ni, Co, Fe) monolayers were modelled by $2 \times 4(001)$ periodic slabs using supercells (consisting of 16 MOOH units) with a vacuum layer of more than 20 Å placed along the z direction. The surface Brillouin zone was sampled with a $3 \times 3 \times 1$ Monkhorst–Pack k-point mesh. The total energy was converged to 10^{-5} eV for each electronic step using the self-consistent field method. All atoms were allowed to relax during the structure optimization until the force on each atom was below 0.03 eV Å^{-1}. Bader charge analysis was conducted to analyse the charge populations[62]. The XANES spectra were calculated using the ab initio multiple scattering code FEFF9[63] based on the optimized geometries to help interpret the experimental results.

To evaluate the adsorption energy of the Fe species on a surface site (denoted by *) we chose the solvated $\mathrm{Fe(OH)_3(H_2O)_3}$ molecular complex as a reference, in which Fe has sixfold coordination and a formal charge state of +3. The adsorption reaction can be written as:

$$* + \mathrm{Fe(OH)_3(H_2O)_3} \rightarrow \mathrm{Fe(OH)_3}^* + 3\mathrm{H_2O}$$

The differential Fe adsorption energy ($\Delta G_{\mathrm{Fe\text{-}M}}$) on a metal oxyhydroxide surface is calculated as follows:

$$\Delta G_{\mathrm{Fe-M}} = G_{(n+1)\mathrm{Fe}^*} - G_{(n)\mathrm{Fe}^*} - G_{\mathrm{Fe-mol}} + 3G_{\mathrm{H2O-mol}}$$

where n represents the number of Fe complexes adsorbed on the surface per supercell and $G_{(n+1)\mathrm{Fe}^*}$, $G_{(n)\mathrm{Fe}^*}$, $G_{\mathrm{Fe-mol}}$ and $G_{\mathrm{H2O-mol}}$ represent the free energies of the surface cell with $n+1$ adsorbed Fe species, the surface cell with n adsorbed Fe species, an $\mathrm{Fe(OH)_3(H_2O)_3}$ molecular complex and a $\mathrm{H_2O}$ molecule in solution under standard conditions, respectively. The average Fe adsorption energy ($\Delta\bar{G}_{\mathrm{Fe-M}}$) on a metal oxyhydroxide surface is calculated as follows:

$$\Delta\bar{G}_{\mathrm{Fe-M}} = (G_{(n)\mathrm{Fe}^*} - G_*)/n - G_{\mathrm{Fe-mol}} + 3G_{\mathrm{H2O-mol}}$$

where G_* represents the free energy of the surface cell without adsorbed Fe species.

The total electronic energy of each system was obtained from the electronic structure calculation in VASP. The free energy was calculated by adding a Gibbs free-energy correction (including contributions from the zero-point energy, enthalpy and entropy) to the total energy calculated in VASP. The Gibbs free-energy corrections were calculated at 25 °C using the standard statistical mechanical model after frequency calculations in VASP. For surface systems, calculated vibrational frequencies were used for the free-energy corrections. For the molecular Fe complex, entropy contributions, including vibrational, translational and rotational contributions, were taken into account. Solvation effects were taken into account using the implicit solvent model to calculate the solvation energy in VASP. For the $\mathrm{H_2O}$ molecule in the liquid phase, the free-energy correction was calculated using the equivalent gas-phase free-energy contribution at a saturated vapour pressure of 3534 Pa (ref. [64]). The calculated free-energy corrections are listed in Supplementary Tables 2–4. The structural information generated in the DFT calculations is shown at the end of Supplementary Data 1.

Data availability

All data are available in the main text, Supplementary Information and Source Data files. Data generated from DFT calculations can be found in Supplementary Data 1.

Received: 22 August 2019; Accepted: 7 February 2020;
Published online: 16 March 2020

References

1. Stamenkovic, V. R., Strmcnik, D., Lopes, P. P. & Markovic, N. M. Energy and fuels from electrochemical interfaces. *Nat. Mater.* **16**, 57–69 (2016).
2. Uhlig, H. H. *Corrosion and corrosion control.* (Wiley: 1985).
3. Peng, Z., Freunberger, S. A., Chen, Y. & Bruce, P. G. A reversible and higher-rate Li-$\mathrm{O_2}$ battery. *Science* **337**, 563–566 (2012).
4. Lim, H. et al. Reaction chemistry in rechargeable Li-$\mathrm{O_2}$ batteries. *Chem. Soc. Rev.* **46**, 2873–2888 (2017).
5. She, Z. W. et al. Combining theory and experiment in electrocatalysis: insights into materials design. *Science* **355**, eaad4998 (2017).
6. Rossmeisl, J., Qu, Z. W., Zhu, H., Kroes, G. J. & Norskov, J. K. Electrolysis of water on oxide surfaces. *J. Electroanal. Chem.* **607**, 83–89 (2007).
7. Seitz, L. C. et al. A highly active and stable IrO_x/$\mathrm{SrIrO_3}$ catalyst for the oxygen evolution reaction. *Science* **353**, 1011–1014 (2016).
8. Man, I. C. et al. Universality in oxygen evolution electrocatalysis on oxide surfaces. *ChemCatChem* **3**, 1159–1165 (2011).
9. Kim, J. S., Kim, B., Kim, H. & Kang, K. Recent progress on multimetal oxide catalysts for the oxygen evolution reaction. *Adv. Energy Mater.* **8**, 1702774 (2018).
10. Zhang, M., Respinis, M. & Frei, H. Time-resolved observations of water oxidation intermediates on a cobalt oxide nanoparticle catalyst. *Nat. Chem.* **6**, 362–367 (2014).
11. Suntivich, J., May, K. J., Gasteiger, H. A., Goodenough, J. B. & Shao-Horn, Y. A perovskite oxide optimized for oxygen evolution catalysis from molecular orbital principles. *Science* **334**, 1383–1385 (2011).
12. Fabbri, E. et al. Dynamic surface self-reconstruction is the key of highly active perovskite nano-electrocatalysts for water splitting. *Nat. Mater.* **16**, 925–931 (2017).
13. Trotochaud, L., Young, S. L., Ranney, J. K. & Boettcher, S. W. Nickel iron oxyhydroxide oxygen evolution electrocatalysts: the role of intentional and incidental iron incorporation. *J. Am. Chem. Soc.* **136**, 6744–6753 (2014).
14. Roy, C. et al. Impact of nanoparticle size and lattice oxygen on water oxidation on $\mathrm{NiFeO}_x\mathrm{H}_y$. *Nat. Catal.* **1**, 820–829 (2018).
15. Zhang, B. et al. Homogeneously dispersed multimetal oxygen-evolving catalysts. *Science* **352**, 333–337 (2016).
16. Dionigi, F. & Strasser, P. NiFe-based (oxy)hydroxide catalysts for oxygen evolution reaction in non-acidic electrolytes. *Adv. Energy Mater.* **6**, 1600621 (2016).
17. Huang, Z. et al. Chemical and structural origin of lattice oxygen oxidation in Co–Zn oxyhydroxide oxygen evolution electrocatalysts. *Nat. Energy* **4**, 329–338 (2019).
18. Strmcnik, D. et al. The role of non-covalent interactions in electrocatalytic fuel-cell reactions on platinum. *Nat. Chem.* **1**, 466–472 (2009).
19. Subbaraman, R. et al. Enhancing hydrogen evolution activity in water splitting by tailoring $\mathrm{Li^+}$-$\mathrm{Ni(OH)_2}$-Pt interfaces. *Science* **334**, 1256–1260 (2011).
20. Yang, C., Fontaine, O., Tarascon, J. -M. & Grimaud, A. Chemical recognition of active oxygen species on the surface of oxygen evolution reaction electrocatalysts. *Angew. Chem. Int. Ed.* **129**, 8778–8782 (2017).
21. Garcia, A. C., Touzalin, T., Nieuwland, C., Perini, N. & Koper, M. T. M. Enhancement of oxygen evolution activity of nickel oxyhydroxide by electrolyte alkali cations. *Angew. Chem. Int. Ed.* **58**, 12999–13003 (2019).
22. Danilovic, N. et al. Activity–stability trends for the oxygen evolution reaction on monometallic oxides in acidic environments. *J. Phys. Chem. Lett.* **5**, 2474–2478 (2014).
23. Chang, S. H. et al. Functional links between stability and reactivity of strontium ruthenate single crystals during oxygen evolution. *Nat. Commun.* **5**, 4191 (2014).
24. Danilovic, N. et al. Using surface segregation to design stable Ru-Ir oxides for the oxygen evolution reaction in acidic environments. *Angew. Chem. Int. Ed.* **53**, 14016–14021 (2014).
25. Gabbri, E. & Schmidt, T. J. Oxygen evolution reaction—the enigma in water electrolysis. *ACS Catal.* **8**, 9765–9774 (2018).
26. Binninger, T. et al. Thermodynamics explanation of the universal correlation between oxygen evolution activity and corrosion of oxide catalysts. *Sci. Rep.* **5**, 12167 (2015).
27. Kim, Y. et al. Balancing activity, stability and conductivity of nanoporous core-shell iridium/iridium oxide oxygen evolution catalysts. *Nat. Commun.* **8**, 1449 (2017).
28. Lopes, P. P. et al. Relationships between atomic level surface structure and stability/activity of platinum surface atoms in aqueous environments. *ACS Catal.* **6**, 2536–2544 (2016).
29. Frydendal, R. et al. Benchmarking the stability of oxygen evolution reaction catalysts: the importance of monitoring mass losses. *ChemElectroChem* **1**, 2075–2081 (2014).
30. Geiger, S. et al. The stability number as a metric for electrocatalyst stability benchmarking. *Nat. Catal.* **1**, 508–515 (2018).
31. Lutterman, D. A., Surendranath, Y. & Nocera, D. G. A self-healing oxygen-evolving catalyst. *J. Am. Chem. Soc.* **131**, 3838–3839 (2009).
32. Huynh, M., Bediako, D. K. & Nocera, D. G. A functionally stable manganese oxide oxygen evolution catalyst in acid. *J. Am. Chem. Soc.* **136**, 6002–6010 (2014).
33. Mefford, J. T. et al. Water electrolysis on $\mathrm{La}_{1-x}\mathrm{Sr}_x\mathrm{CoO}_{3-\delta}$ perovskite electrocatalysts. *Nat. Commun.* **7**, 11053 (2016).
34. Grimaud, A. et al. Activating lattice oxygen redox reactions in metal oxides to catalyse oxygen evolution. *Nat. Chem.* **9**, 457–465 (2017).
35. Subbaraman, R. et al. Trends in activity for the water electrolyzer reactions on 3*d* M(Ni,Co,Fe,Mn) hydr(oxy)oxide catalysts. *Nat. Mater.* **11**, 550–557 (2012).
36. Zeng, Z., Chang, K., Kubal, J., Markovic, N. M. & Greeley, J. Stabilization of ultrathin (hydroxyl)oxide films on transition metal substrates for electrochemical energy conversion. *Nat. Energy* **2**, 17070 (2017).
37. Corrigan, D. A. The catalysis of the oxygen evolution reaction by iron impurities in thin film nickel oxide electrodes. *J. Electrochem. Soc.* **134**, 377–384 (1987).
38. Subbaraman, R. et al. Origin of anomalous activities for electrocatalysts in alkaline electrolytes. *J. Phys. Chem. C.* **116**, 22231–22237 (2012).

39. Wang, J. et al. In situ formation of molecular Ni-Fe active sites on heteroatom-doped graphene as a heterogeneous electrocatalyst toward oxygen evolution. *Sci. Adv.* **4**, eaap7970 (2018).
40. Burke, M. S. et al. Revised oxygen evolution reaction activity trends for first-row transition-metal (oxy)hydroxides in alkaline media. *J. Phys. Chem. Lett.* **6**, 3737–3742 (2015).
41. Burke, M. S. et al. Oxygen evolution reaction electrocatalysis on transition metal oxides and (oxy)hydroxides: activity trends and design principles. *Chem. Mater.* **27**, 7549–7558 (2015).
42. Zou, S. et al. Fe (oxy)hydroxide oxygen evolution reaction electrocatalysis: intrinsic activity and the roles of electrical conductivity, substrate, and dissolution. *Chem. Mater.* **27**, 8011–8020 (2015).
43. Li, N. et al. Influence of iron doping on tetravalent nickel content in catalytic oxygen evolving films. *Proc. Natl Acad. Sci. USA* **114**, 1486–1491 (2017).
44. Görlin, M. et al. Oxygen evolution reaction dynamics, faradaic charge efficiency, and the active metal redox states of Ni–Fe oxide water splitting electrocatalysts. *J. Am. Chem. Soc.* **138**, 5603–5614 (2016).
45. Friebel, D. et al. Identification of highly active Fe sites in (Ni,Fe)OOH for electrocatalytic water splitting. *J. Am. Chem. Soc.* **137**, 1305–1313 (2015).
46. Chen, J. Y. C. et al. Operando analysis of NiFe and Fe oxyhydroxide electrocatalysts for water oxidation: detection of Fe^{4+} by Mössbauer spectroscopy. *J. Am. Chem. Soc.* **137**, 15090–15093 (2015).
47. Xiao, H., Shin, H. & Goddard, W. A. Synergy between Fe and Ni in the optimal performance of (Ni,Fe)OOH catalysts for the oxygen evolution reaction. *Proc. Natl Acad. Sci. USA* **115**, 5872–5877 (2018).
48. Goldsmith, Z. K. et al. Characterization of NiFe oxyhydroxide electrocatalysts by integrated electronic structure calculations and spectroelectrochemistry. *Proc. Natl Acad. Sci. USA* **114**, 3050–3055 (2017).
49. Stevens, M. B., Trang, C. D. M., Enman, L. J., Deng, J. & Boettcher, W. Reactive Fe-sites in Ni/Fe (oxy)hydroxide are responsible for exceptional oxygen electrocatalysis activity. *J. Am. Chem. Soc.* **139**, 11361–11364 (2019).
50. Song, F. et al. An unconventional iron nickel catalyst for the oxygen evolution reaction. *ACS Cent. Sci.* **5**, 558–568 (2019).
51. Diaz-Morales, O., Ledezma-Yanz, I., Koper, M. T. M. & Calle-Vallejo, F. Guidelines for the rational design of Ni-based double hydroxide electrocatalysts for the oxygen evolution reaction. *ACS Catal.* **5**, 5380–5387 (2015).
52. Bard, A. J. & Faulkner, L. R. *Electrochemical Methods* (Wiley, 2001).
53. Hammer, B. & Norskov, J. K. Theoretical surface science and catalysis—calculations and concepts. *Adv. Catal.* **45**, 71–129 (2000).
54. McCrory, C. C. L., Jung, S., Peters, J. C. & Jaramillo, T. F. Benchmarking heterogeneous electrocatalysts for the oxygen evolution reaction. *J. Am. Chem. Soc.* **135**, 16977–16987 (2013).
55. Rhee, C. K. et al. Osmium nanoislands spontaneously deposited on a Pt(111) electrode: an XPS, STM and GIF-XAS study. *J. Electroanal. Chem.* **554**, 367–378 (2003).
56. Kresse, G. & Furthmuller, J. Efficient iterative schemes for *ab initio* total-energy calculations using a plane-wave basis set. *Phys. Rev. B* **54**, 11169–11186 (1996).
57. Mathew, K., Sundararaman, R., Letchworth-Weaver, K., Arias, T. A. & Henning, R. G. Implicit solvation model for density-functional study of nanocrystal surfaces and reaction pathways. *J. Chem. Phys.* **140**, 084106 (2014).
58. Mathew, K., Chaitanya Kolluru, V. S., Mula, S., Steinmann, S. N. & Henning, R. G. Implicit self-consistent electrolyte model in plane-wave density-functional theory. *J. Chem. Phys.* **151**, 234101 (2019).
59. Perdew, J. P., Burke, K. & Ernzerhof, M. Generalized gradient approximation made simple. *Phy. Rev. Lett.* **77**, 3865–3868 (1996).
60. Grimme, S. Semiempirical GGA-type density functional constructed with a long-range dispersion correction. *J. Comput. Chem.* **27**, 1787–1799 (2006).
61. Durarev, S. L., Botton, G. A., Savrasov, S. Y., Humphreys, C. J. & Sutton, A. P. Electron-energy-loss spectra and structural stability of nickel oxide: an LSDA+U study. *Phys. Rev. B* **57**, 1505–1509 (1998).
62. Sanville, E., Kenny, S. D., Smith, R. & Henkelman, G. Improved grid-based algorithm for bader charge allocation. *J. Comput. Chem.* **28**, 899–908 (2007).
63. Rehr, J. J., Kas, J. J., Vila, F. D., Prange, M. P. & Jorissen, K. Parameter-free calculatons of X-ray spectra with FEFF9. *Phys. Chem. Chem. Phys.* **12**, 5503–5513 (2010).
64. Peterson, A. A. & Norskov, J. K. Activity descriptor for CO_2 electroreduction to methane on transition-metal catalysts. *J. Phys. Chem. Lett.* **3**, 251–258 (2012).

Acknowledgements

The research was carried out at Argonne National Laboratory and supported by the Office of Science, Office of Basic Energy Sciences, Materials Sciences and Engineering Division. Use of the Center for Nanoscale Materials and the Advanced Photon Source, Office of Science user facilities, was supported by the US Department of Energy, Office of Science, Office of Basic Energy Sciences, under contract no. DE-AC02-06CH11357. T.K. thanks the Japan Society for the Promotion of Science for Postdoctoral Fellowship. H.H. acknowledges the funding support from the Visiting Faculty Program of the Department of Energy.

Author contributions

D.Y.C., P.P.L. and N.M.M. designed the experiments. D.Y.C., P.P.L. and P.F.B.D.M. conducted the electrochemical measurements and analysis. H.H. and P.Z. performed DFT calculations and analysis. D.Y.C., T.K., H.Y., S.S. and S.L. conducted in situ XANES measurements and analysis. D.T. and Y.Z. carried out STM and AFM analyses. D.S. and V.R.S. discussed and commented on the results. D.Y.C., P.P.L., P.Z. and N.M.M. wrote the manuscript. All authors approved the final version of the manuscript.

Competing interests

The authors declare no competing interests.

Additional information

Supplementary information is available for this paper at https://doi.org/10.1038/s41560-020-0576-y.

Correspondence and requests for materials should be addressed to N.M.M.

Reprints and permissions information is available at www.nature.com/reprints.